Recent advances in blazed grating fabrication by electron-beam lithography

Daniel W. Wilson, Paul D. Maker, Richard E. Muller, Pantazis Mouroulis, and Johan Backlund
Jet Propulsion Laboratory
California Institute of Technology
Pasadena, California 91109

ABSTRACT

Convex and concave diffraction gratings are required for concentric imaging spectrometer forms. Direct-write electron-beam lithography has proven to be an effective method for fabricating high-efficiency blazed gratings on non-flat substrates. Recently fabricated convex gratings have demonstrated relative efficiency greater than 90%, diffuse scatter and ghosts less than $5x10^{-4}$ of the main diffraction order, and zeroth-order wavefront error less than ¼-wave at 633 nm. Such gratings can be fabricated on JPL's JEOL JBX-9300FS electron-beam lithography system with a writing speed of approximately 1 to 2 cm^2 per hour. The technique was recently used to fabricate flight-qualified gratings for the Compact Reconnaissance Imaging Spectrometer for Mars (CRISM) instrument that is scheduled to fly on the NASA Mars Reconnaissance Orbiter in 2005.

Keywords: electron-beam lithography, diffraction gratings, imaging spectrometers

1. INTRODUCTION

Concentric imaging spectrometer forms have become popular in recent years owing to their compact size and high-performance.[1-4] A difficulty with these imaging spectrometer designs, however, is that they require either a convex or concave grating with relatively low groove density (typically 10-100 lines/mm). If high efficiency is desired, then the grating must be accurately blazed. The combination of the non-flat substrate and the low groove density make the fabrication process challenging for techniques such as diamond ruling or holography followed by ion-beam etching.

We have developed techniques for fabricating high-performance blazed gratings on non-flat substrates using direct-write electron-beam lithography.[5-7] We recently upgraded our electron-beam lithography system from a JEOL JBX-5DII (referred to hereafter as 5DII) to a JEOL JBX-9300FS (referred to hereafter as 9300FS). This required a number of changes in our technique for writing analog surface-relief profiles on non-flat substrates. In Sec. 2, we describe the electron-beam tool calibration and non-flat blazed grating fabrication process. In Sec. 3, we give results from scattering measurements of gratings fabricated on the 5DII and 9300FS tools. In Sec. 4, we describe the fabrication and characterization of one of the flight-qualified gratings for the Compact Reconnaissance Imaging Spectrometer for Mars (CRISM) instrument that is scheduled to fly on the NASA Mars Reconnaissance Orbiter in 2005. In Section 5, we summarize and point to future improvements that can be made.

2. BLAZED GRATING FABRICATION AND E-BEAM SYSTEM CALIBRATION

The upgrade from the 5DII to the 9300FS posed a number of challenges to our process for fabricating non-flat blazed gratings. Table I summarizes the important differences and their impacts. The 9300FS is a vastly superior tool compared to the 5DII, but the smaller spot size produced by the field-emission source requires closer spot-to-spot spacing to maintain good smoothness of the exposed resist. Also, the dual-deflector system on the 9300FS requires accurate calibration of the main- and sub-deflectors to avoid field- and subfield stitching defects in the gratings. As will be discussed in Secs. 2.1 and 3, such defects produce undesirable ghost diffraction orders.

Table 1. Important E-beam parameters for analog-relief lithography

Parameter	JEOL JBX-5DII (previous system)	JEOL JBX-9300FS (current system)	Fabrication Process Impact
1. Accelerating voltage	50 kV	100 kV	Decreased resist sensitivity, hence increased required dose. Increased range of proximity effect makes compensation techniques more accurate. Increased electron penetration depth permits fabrication of deeper grooves.
2. Electron source	LaB_6 crystal	ZrO/W field-emission	Much smaller spot size for the same current. Spots must be placed closer together to maintain low surface roughness.
3. Deflector system	Single-deflector, dual digital-to-analog converter	Dual-deflector, dual digital-to-analog converter	Must accurately calibrate both deflectors to avoid stitching defects
4. Scan speed	2 MHz	25 MHz	Faster grating exposures, although parameters 1 and 2 above decrease achievable speed

2.1. Fabrication of analog surface-relief profiles in electron-beam resist

Our technique for fabricating analog surface-relief profiles in E-beam resist has been described previously,[8-14] but we will review it here to illustrate differences with the 9300FS. To start, the desired depth profile is represented by an array of square or rectangular pixels whose size is a small fraction of the groove width . Each pixel will ultimately be exposed with the E-beam at the same accelerating voltage, but with a dwell time that is proportional to the desired depth. The resulting dose increases the solubility of the resist to developer, and with careful monitoring of the depth as a function of development time, surface profiles with less than 5% error can be fabricated. For reflective gratings, the resist is overcoated with an evaporated metal coating, typically aluminum.

In order to calculate the proper pixel doses, two main physical effects must be calibrated and compensated: (1) the nonlinear dose sensitivity of the resist/developer combination, and (2) the proximity effect—exposure resulting from electrons back-scattered from underlying resist and the substrate. The increase to 100 kV accelerating voltage on the 9300FS required that we recalibrate these two effects for all our resist and substrate combinations. At JPL we have developed analog relief fabrication processes for polymethylmethacrylate (PMMA)[15] developed in pure acetone and for polymethylglutarimide (PMGI)[16] developed in several standard alkaline developers. Figure 1 shows the broad-area depth vs. dose response for PMMA exposed at 100kV and developed for 15 seconds in pure acetone. The fitted curve is used to assign doses to the pixels representing the desired depth profile.

The next pattern preparation step is to compensate for the proximity effect. This is critical since typically one-third to one-half of the total dose comes from the backscattered electrons. The proximity effect is commonly described by a Gaussian model, and the dose point-spread function can be represented as

$$PSF(\mathbf{r}) = \delta(\mathbf{r}) + \frac{\eta}{\pi\alpha^2}\exp(-r^2/\alpha^2) \qquad (1)$$

where η is the strength and α is the range. The incident beam can be represented as a delta function in Eq. (1) because the range of the proximity effect is large compared to the beam diameter and we are not concerned with correcting feature sizes on the order of the beam size. The total dose delivered to the resist is thus the primary (incident) dose convolved with the point-spread function. To characterize the proximity effect, we use a scanning probe microscope (SPM) to profile the edges of the same large area uniform exposures that are used to characterize the resist nonlinearity in Fig. 1(a). Figure 1(b) shows an SPM scan of PMMA exposed with 120 $\mu C/cm^2$ and developed for 15 seconds in pure acetone. The abrupt step is the edge of the primary dose pattern. The total dose delivered to the resist is the convolution of the primary dose pattern and the PSF. For the case of a broad area exposure, the dose at the edge can be derived analytically as the convolution of Eq. (1) with a step function to give

$$D_{tot}(x) = D_{prim}\left\{\text{step}(x - x_{step}) + \frac{\eta}{2}\left[1 + \text{erf}\left(\frac{x - x_{step}}{\alpha}\right)\right]\right\} \quad (2)$$

where D_{prim} is the value of the uniform primary dose. To fit the AFM profile and determine the proximity effect range and strength parameters, Eq. (2) is converted to depth using the nonlinear depth function from Fig. 1(a), with the dose axis scaled by $(1+\eta)$ to account for the fact that for broad area exposures, $D_{tot} = D_{prim}(1 + \eta)$. Table 2 shows representative proximity effect parameters for PMMA on different substrate materials for exposure at 50 kV (5DII) and at 100 kV (9300FS). For most substrates, the major effect is that the range increases by a factor between 3 and 4. In some cases, fitting was difficult and the strength parameter has significant uncertainty.

(a)

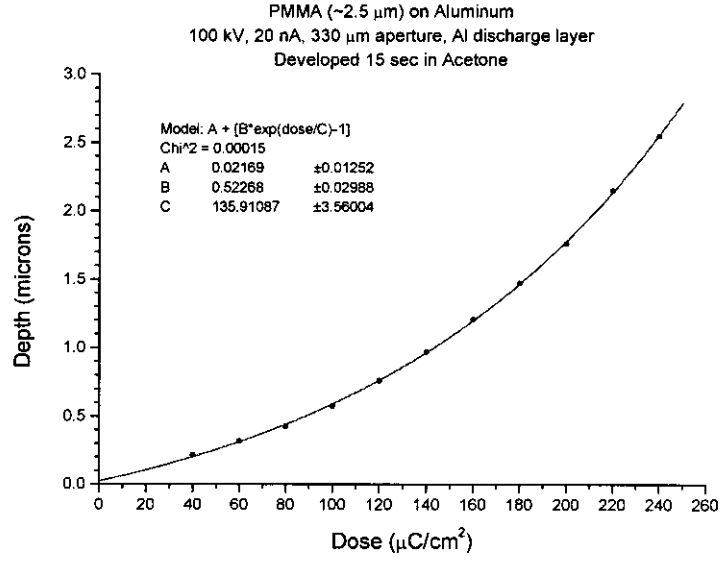

(b)

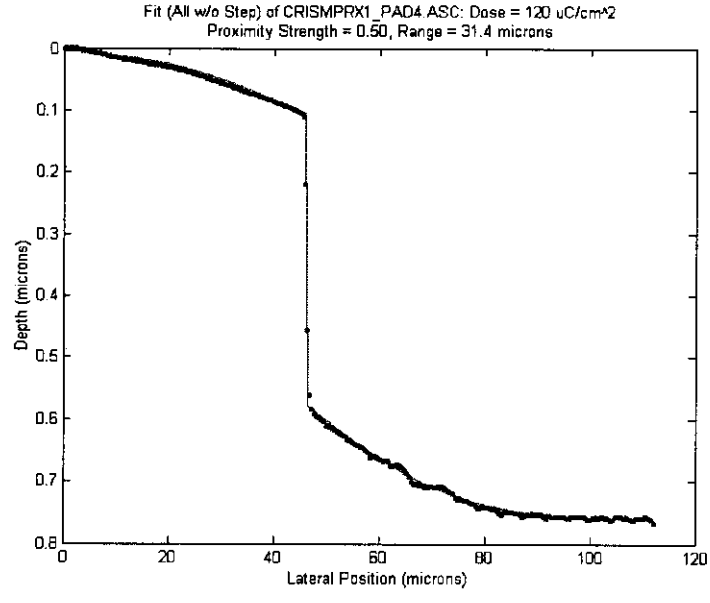

Figure 1. (a) Nonlinear depth vs. dose sensitivity of PMMA on aluminum (100 kV, 15 seconds acetone development). (b) scanning probe microscope profile of the edge of a uniform dose exposure of same PMMA as in (a). The solid line is a fit of Eq. (2) converted to depth, with strength η and range α as parameters.

Table 2. Proximity effect parameters

Substrate (PMMA resist)	50 kV (JEOL JBX5DII)		100 kV (JEOL JBX-9300FS)	
	Strength	Range (μm)	Strength	Range (μm)
Fused Silica	0.50	10.7	0.5	37
Aluminum	0.47	9.3	0.5	31
Silicon	0.48	10.6	0.55	41
GaAs	0.93	6.0	0.7	20

Once the proximity effect parameters are known, the required primary dose for each pixel can be determined by deconvolving Eq. (2) from the desired total dose pattern. In practice, this is performed using fast Fourier transform computations. Deconvolution of steps in the desired depth profile produces non-realizable negative doses. The solution is to recess the entire depth profile until no negative doses are required (typically 0.2 to 0.4 μm). The final pattern preparation step is to convert the pattern of primary pixel doses into the native JEOL E-beam format using JPL in-house software.

The manner in which the pixel pattern is exposed by the 9300FS impacts the optical performance of the grating. Each pixel is exposed using multiple overlapping spots of diameter less than 100 nm to achieve a smooth surface. Larger spots would be desirable, but 100 nm is the approximate limit of our current 9300FS configuration. The spot spacing on the 9300FS must be an integral number of nanometers (unless fine-pitch control is used), and each pixel must be an integral number of spots. The 9300FS uses a high-speed deflector to scan small areas up to 4 μm square that we term "subfields". For grating fabrication, the pixels are usually very narrow perpendicular to the groove (typ. <0.5 μm) but long parallel to the groove, so the subfields are 1 pixel wide and several microns long. Figure 2 shows a typical grating writing pattern with the subfield arrangement as an inset on the right. The low-speed sub-deflector positions the subfields within the "field"—the square region (500 μm maximum) over which the stage does not move. The interferometrically controlled stage has a field-to-field stitching specification of 20 nm, which we have confirmed by exposing vernier patterns. However, at the field boundaries, the pixels on one side are exposed with a beam that is opposite in incident angle to those on the other side, so for finite thickness resist films, there will always be some exposure error. Analog relief lithography is exquisitely sensitive to exposure errors, and hence field and sub-field boundaries become dents and bumps in the resist if they are not perfect. Because the field and subfield boundaries are periodic, they produce optical "ghost" diffraction orders. If there are M subfields per grating groove, then the sub-field ghosts will be coincident with the orders $\pm M$, $\pm 2M$, $\pm 3M$.... Considering that there are usually 20 or more pixels (subfields) per groove, and in most cases the pixels are subwavelength in width, these ghosts (if they propagate) are negligible. In the direction parallel to the grooves, the subfields can be up to 4 μm, so the subfield ghosts perpendicular to the diffraction direction will be closer to the main orders, but they are generally still far enough away to be negligible. The field boundaries produce ghosts that are the main concern. If a grating is exposed with N grating grooves (periods) per field, then there will be $N - 1$ ghosts in between the main diffraction orders. In Sec. 4, we will show measurements of typical field ghosts. If field ghosts are a severe concern for a particular application, then we have a variety of field-shift writing techniques[17-20] available that can be used to reduce their intensity. However, these techniques sacrifice writing speed, so they are used only if necessary. So far, we have not found the need.

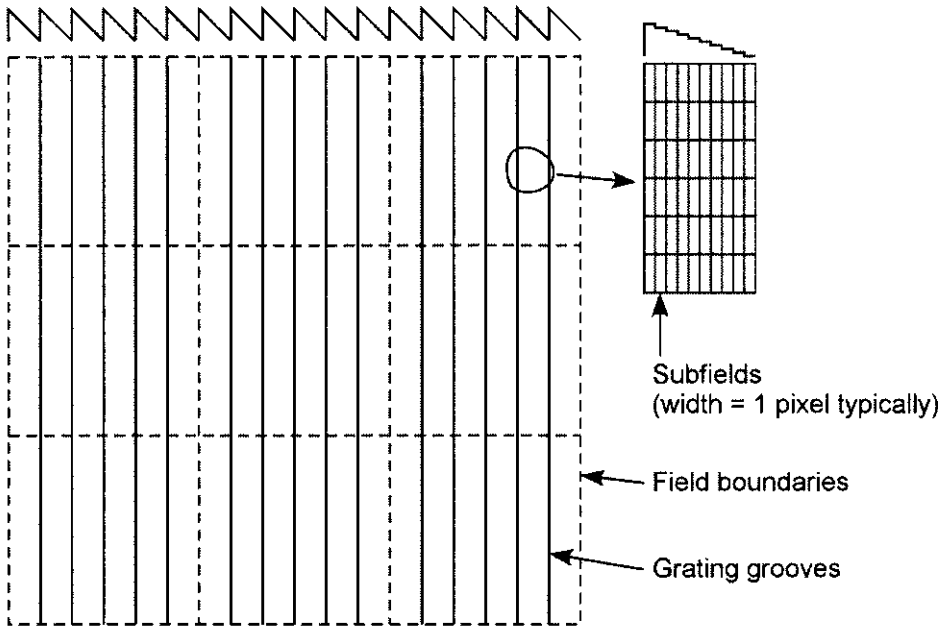

Figure 2. Typical E-beam writing pattern for blazed grating fabrication

2.2. Electron-beam system calibration for writing on non-flat substrates

The JPL 9300FS has been specially modified by JEOL to allow writing on substrates with approximately 3.5 mm of height variation. This is termed the "sag" of the substrate, which for convex substrates is the dome to grating edge height. Accurate E-beam exposure on non-flat substrates is possible because the beam has significant depth of field (10's of μm) in its focus and pattern distortion parameters. The concept is straightforward—split the pattern up into 'zones' that correspond to substrate regions where the height changes by one depth-of-field as shown in Fig. 3. For spherical convex or concave substrates, these zones are annular in shape. The annular zone patterns are then exposed sequentially, adjusting the E-beam column settings for optimal writing at the mid-height of each zone. The local deflection coefficients do, however, change as the height changes across the zone, by a factor equal to the ratio of the zone height step to the 9300FS working distance. This factor, ~50μm / 7cm = 1/1400, not only gives rise to what appear to be field stitch errors, but limits the grating pitch precision and hence the ultimate resolution of the target spectrometer. The effect can be lessened by using more zones with smaller steps. Great care must be exercised in determining the height-dependent column settings. We accomplish the calibration in the following manner. First, gold fiducial crosses are fabricated on a spherical convex substrate (lens) that has sag approximately equal to the maximum range of the E-beam system. This step is performed by focusing the E-beam at the center height and exposing as if the substrate were flat. Writing errors do occur, but the crosses require only low-resolution binary lithography. Next, the beam is manually focused on each cross to determine the focus setting as a function of height. The E-beam deflector calibration routine is run on each cross to determine functions for the x- and y-gain and x- and y-rotation settings for both the main- and sub-deflectors of the 9300FS. Once the height functions for the column settings are known, they can be used to determine parameters for a jobdeck HEIGHT command that is called before each zone pattern is exposed. This calibration procedure need only be performed after major column maintenance operations. For grating fabrication, a substrate having the same radius of curvature as the grating is height-mapped by focusing on silver or gold particles applied to the surface. This is necessary because the mounts for each grating job are unique and the absolute height can vary from the design.

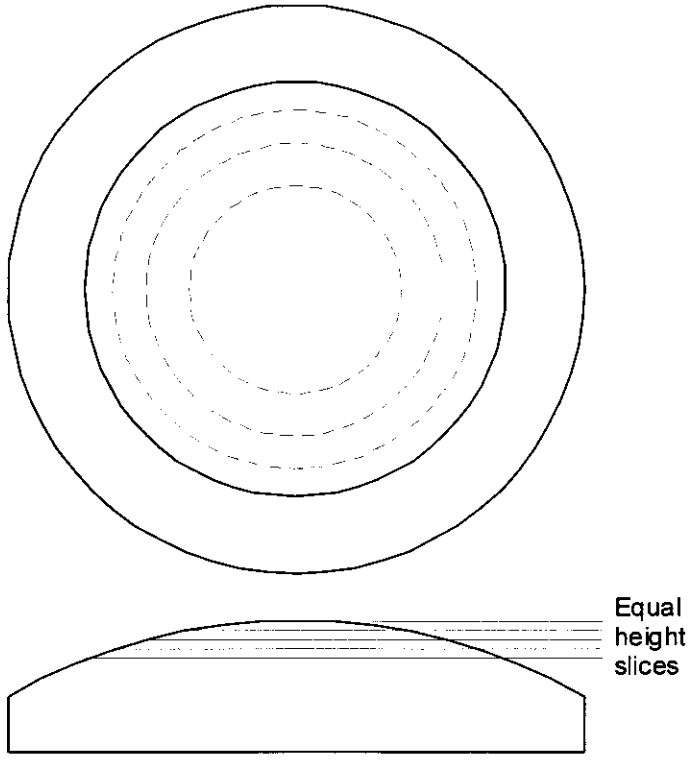

Figure 3. Pattern division scheme for E-beam exposure on non-flat substrates.

3. GRATING SCATTERING MEASUREMENTS

In an earlier publication, we described the excellent diffraction efficiency characteristics of E-beam fabricated blazed convex gratings.[5,6] Here we present measurements of the scattering from convex gratings fabricated on both the 5DII and 9300FS E-beam systems. The gratings were identical in design so direct comparison is possible. For both gratings, the grating period was 20 μm, and the field size was 800 μm (the 9300FS was operated in its 50 kV mode, for which the maximum field size is 1000 μm). Figure 4 shows a highly saturated image of the diffraction pattern produced by the 9300FS grating. The image was taken with a charge-injection-device camera to avoid blooming. There are 39 field ghosts between the first and second orders due to the field/period ratio in agreement with the discussion in Sec. 2.2. It is obvious that the ghosts dominate over diffuse scatter. To measure the relative irradiance of the ghosts, a single-mode fiber propagating 633 nm light was used as the input to an Offner reflective spectrometer. A 100 μm slit was then scanned with a photodetector across the diffraction pattern. The result is shown in Fig. 5. The slit is too wide to resolve the field ghosts of the 9300FS grating, but it does resolve the subfield ghosts from the 5DII grating. On the 5DII, the subfield size used for this grating was 100 μm, so there were 4 subfield ghosts between the main orders. To resolve the field ghosts of the 9300FS grating, we used a 5 μm slit and the result is shown in Fig. 6. These and other measurements indicate the relative irradiance of the ghosts and diffuse scatter does not exceed 5×10^{-4} of the main diffraction order.

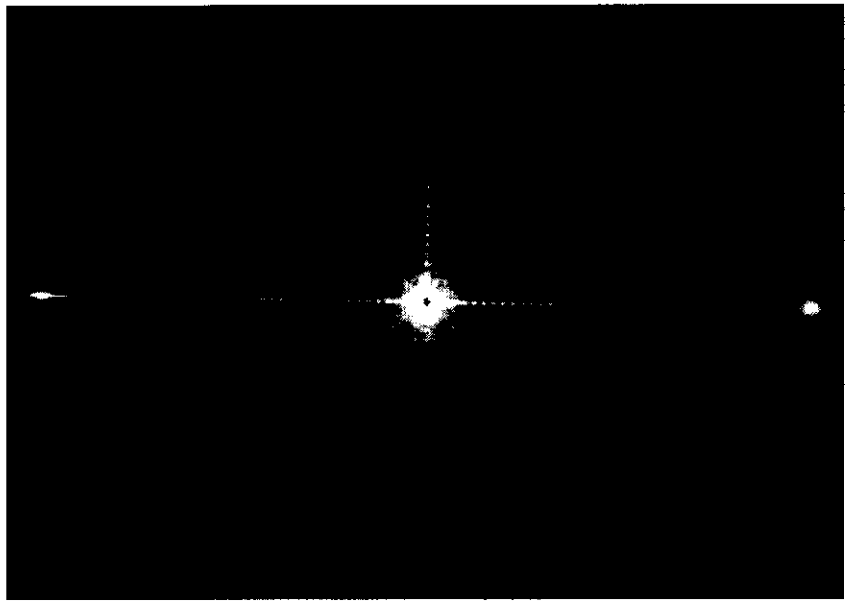

Figure 4. Highly saturated image of diffraction pattern produced by a convex grating fabricated using the JEOL JBX-9300FS. The spots between the main orders are due to the periodic field-stitching errors.

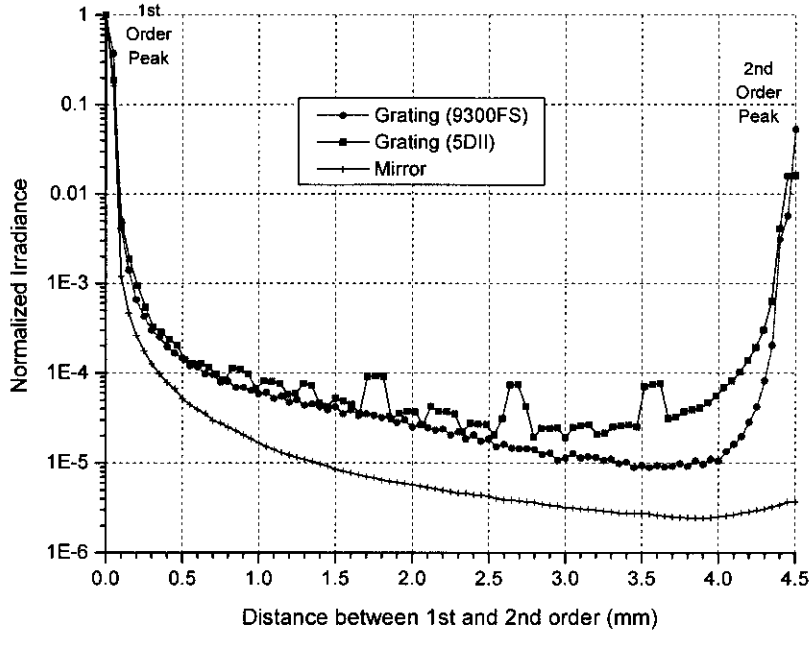

Figure 5. Measurement of irradiance between orders by scanning a 100 μm slit for convex gratings fabricated on the 9300FS and 5DII E-beam systems.

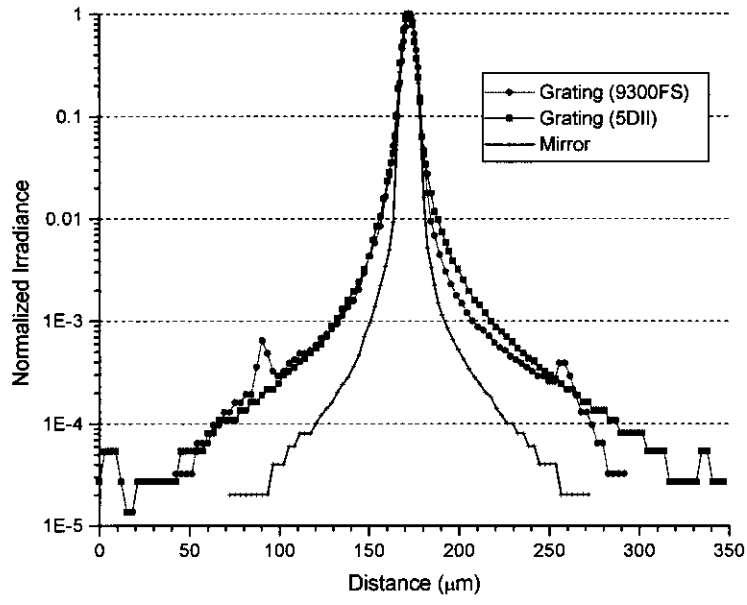

Figure 6. Measurement of irradiance near the main (first) order by scanning a 5 μm slit for convex gratings fabricated on the 9300FS and 5DII E-beam systems.

4. FABRICATION OF THE VNIR GRATING FOR CRISM

We recently fabricated flight-qualified convex gratings for the Compact Reconnaissance Imaging Spectrometer for Mars (CRISM) instrument that is scheduled to fly on the NASA Mars Reconnaissance Orbiter in 2005. The spectrometer is being built by SSG Precision Optronics, Inc,. and the instrument is being built by Johns Hopkins University Applied Physics Laboratory. As a case study, we describe the fabrication of the visible near-infrared (VNIR) gratings. Table 3 shows the relevant VNIR grating and E-beam exposure parameters.

Table 3. CRISM VNIR Grating Parameters

Parameter	**Value**
Wavelength range	0.4 to 1.0 μm
Grating period	15.552 μm
Groove angles, depths (dual blaze)	0.77 deg (depth = 0.21 μm), 2.6 deg (depth = 0.71 μm)
Size	Diameter = 0.88 inch (22.4 mm), area = 3.94 cm^2
Radius of curvature, sag	R = 3.49953 inch (88.8881 mm), sag = 0.7 mm
Materials	Diamond-turned aluminum substrate, PMMA resist, 900 Å bare aluminum reflective overcoat
E-beam pixel size	0.192 μm (81 pixels per groove)
E-beam spot spacing	64 nm (3 spots per pixel)
E-beam subfield, field sizes	Subfield = 0.192 μm x 3.84 μm (3 x 60 spots) Field = 311.04 μm (20 grooves)
E-beam depth of field, number of annular height zones	Depth of field = 48 μm, Number of zones = 16
E-beam exposure (JEOL JBX-9300FS)	100 kV, 30 nA, 330 μm aperture, 7 hours

Figure 7 shows a photograph if the fabricated grating. The two blaze areas diffract visible light efficiently in different orders, so the reflection of the overhead light appears offset. The shallow area (front-left in photo) is diffracting in first order, and the deep area (back-right in photo) is diffracting in second order. When operating in the spectrometer, the first orders add together coherently (weighted by the area ratios and illumination apodization pattern) to produce the total efficiency.

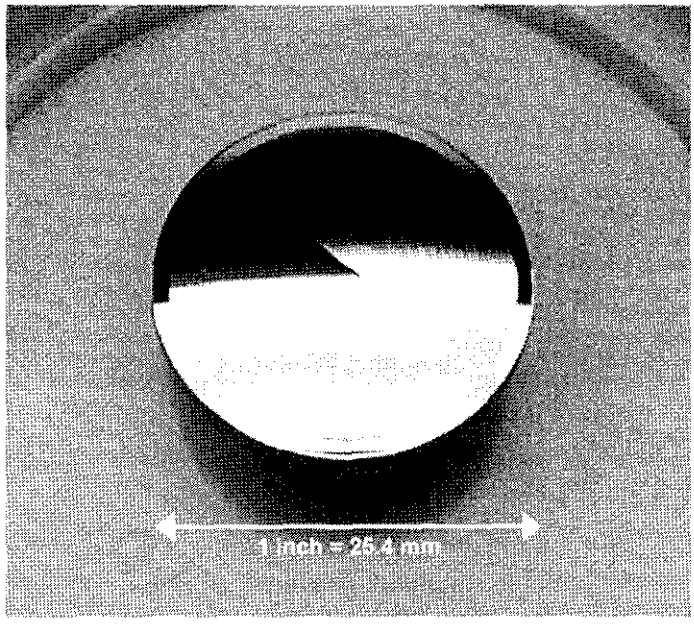

Figure 7. Photograph of a CRISM VNIR grating.

Figure 8 shows a scanning probe microscope profile at the dual-blaze area boundary. The blaze angle of the shallow area was measured to be 0.76 degrees (-1.3% error), and the blaze angle of the deep area was measured to be 2.56 degrees (-1.6% error). Blaze angle measurements were performed at a variety of locations and the errors ranged from -2.2% to 1.3% in the shallow area, and from -1.5% to 2.6% in the deep area. The surface roughness was also measured and varied from ~4 to 9 nm rms in the deep area, and from ~4 to 7 nm rms in the shallow area. Figure 8 also shows how the shallow area was recessed to align the mid-depths of the grooves to minimize wavefront error.[6] A zeroth-order interferogram of the grating is shown in Fig. 9, indicating that the peak-to-valley wavefront error at 633 nm was 0.232 waves.

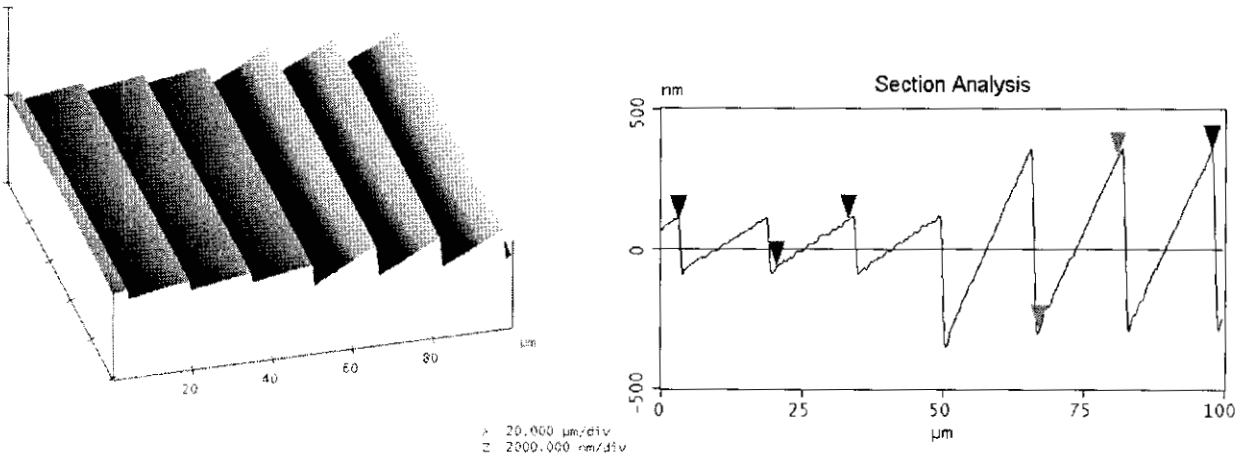

Figure 8. Scanning probe microscope scan at the dual-blaze boundary of the CRISM VNIR grating in Fig. 7.

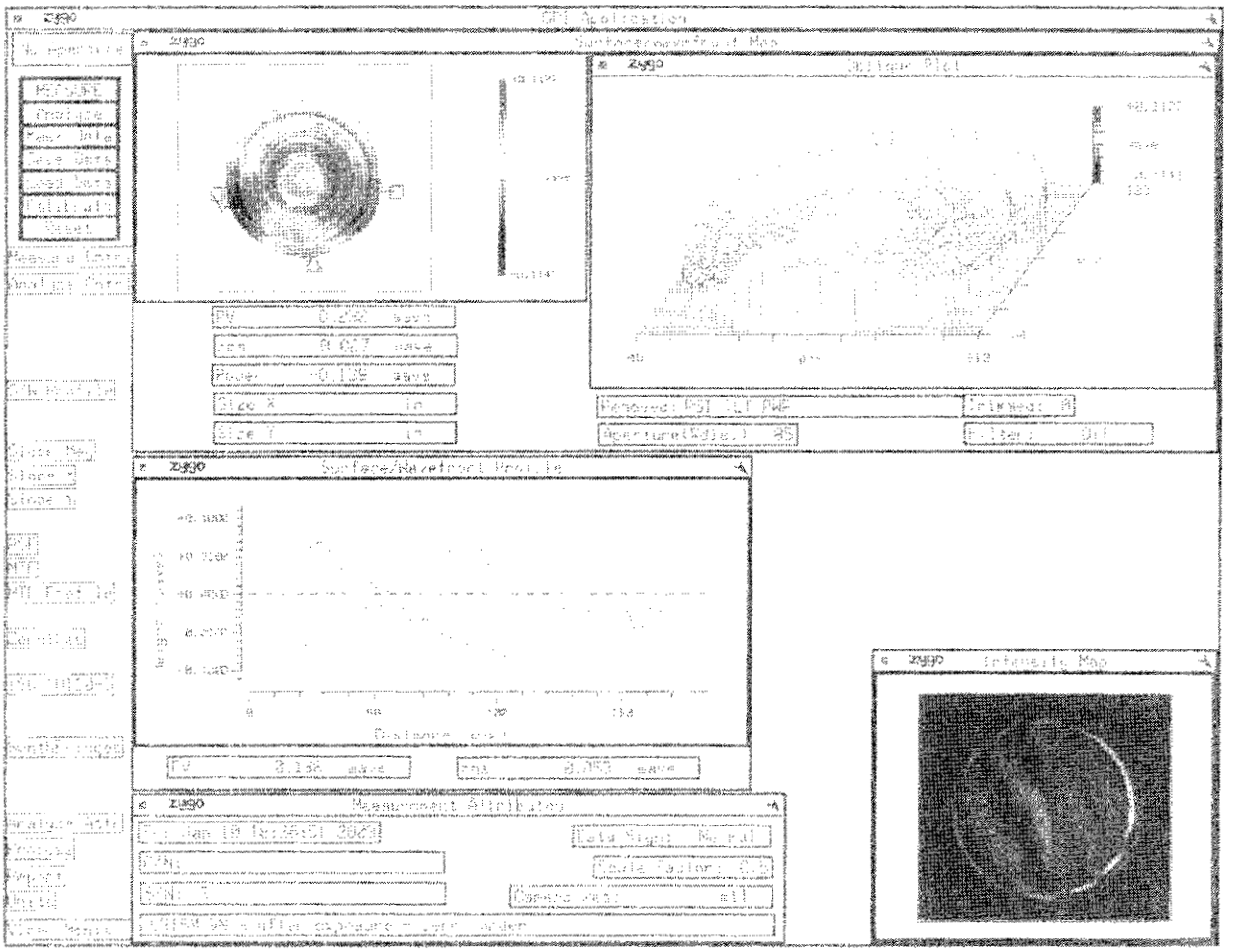

Figure 9. Wavefront-error measurement of the CRISM VNIR grating operating in zeroth-order. The rotationally symmetric error seen is due to the diamond-turned substrate.

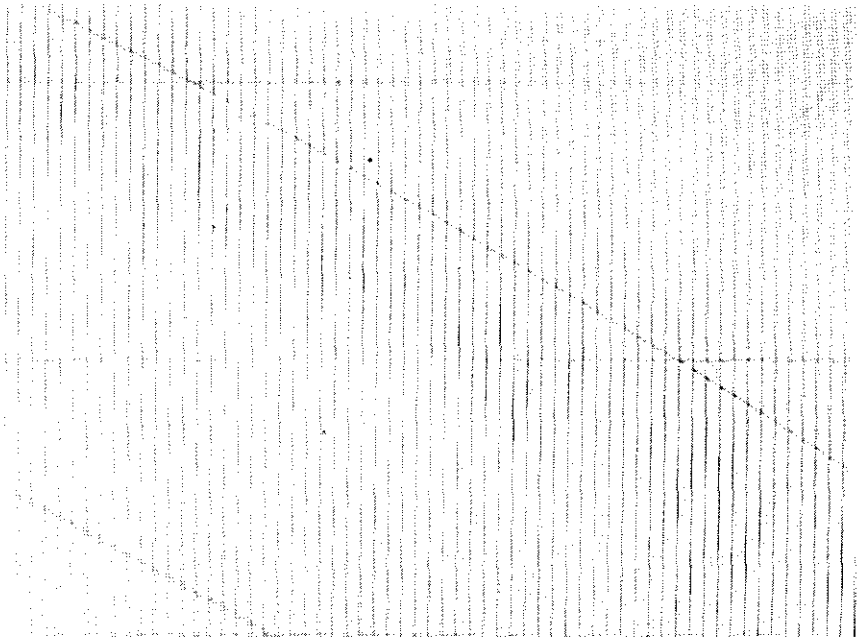

Figure 10. Optical micrograph showing field- and annular-zone boundaries.

Finally, Figure 10 shows an optical micrograph showing the field (horizontal) and annular height-zone boundaries (curved). Note that the field boundary disappears near the middle of the annual zone, indicating that the deflector calibration was optimum at that height. This confirms that our deflector calibration and substrate mapping were accurate.

5. SUMMARY AND FUTURE WORK

Even though our non-flat grating fabrication technique is now fairly mature, there are still improvements to be made. Field stitching is the main source of ghosts, so minimizing the stitching errors is highly desirable. This may be accomplished by using some of the built-in field-shift writing modes of the 9300FS, or we could simply reduce the annular zone size corresponding to the depth of field. A third possibility would be to implement height-shift writing, where we would create two (or more) sets of annular height-zone patterns with the mid-heights of the two sets shifted by one-half of the E-beam depth of field. The grating would then be exposed twice: once at half the dose with first set of patterns, and then again with the other set of patterns. This would tend to average out both field boundaries and annular zone boundaries. The field boundaries could even be displaced one-half field apart in the two patterns to further reduce the amplitude of the periodic defects and hence the ghosts. The drawback of this approach is that the grating would take twice as long to expose.

ACKNOWLEDGEMENTS

We would like to thank Leonard Wayne and Edward Hagerott of JPL for engineering and management support during the CRISM grating project. We would also like to thank JEOL for working with us to enhance the performance of their E-beam systems for this non-standard type of lithography. Finally, we thank Kris Kosakowski of SSG Precision Optronics, Inc. for allowing us to publish the CRISM grating specifications. This research was carried out at the Jet Propulsion Laboratory, California Institute of Technology, under a contract with the National Aeronautics and Space Administration.

REFERENCES

1. L. Mertz: "Concentric spectrographs," Appl. Opt. **16**, 3122-3124 (1977).
2. D. R. Lobb: "Theory of concentric designs for grating spectrometers," Appl. Opt. **33**, 2648-2658 (1994).
3. D. Kwo, G. Lawrence, and M. Chrisp: "Design of a grating spectrometer from a 1:1 Offner mirror system," SPIE Proc. **818**, 275-279 (1987).
4. P. Mouroulis and M. McKerns: "Pushbroom imaging spectrometer with high spectroscopic data fidelity: experimental demonstration," Opt. Eng. **39**, 808-816 (2000).
5. P. D. Maker, R. E. Muller, D. W. Wilson, and P. Mouroulis, "New convex grating types manufactured by electron beam lithography," 1998 OSA Diffractive Optics Topical Meeting, Kailua-Kona, Hawaii, June 8-11 (1998).
6. P. Mouroulis, D. W. Wilson, P. D. Maker, and R. M. Muller, "Convex grating types for concentric imaging spectrometers," *Appl. Optics* **37**, 7200-7208 (1998).
7. P. D. Maker, R. E. Muller, and D. W. Wilson, "Diffractive optical elements on non-flat substrates using electron beam lithography," US Patent. No. 6,480,333, assigned to California Institute of Technology, Pasadena, CA (1998).
8. T. Fujita, H. Nishihara, and J. Koyama, "Fabrication of micro lenses using electron-beam lithography," *Opt. Lett.* **6**, 613-615 (1981).
9. M. Ekberg, M. Larsson, S. Hård, and B. Nilsson, "Multilevel phase holograms manufactured by electron beam lithography," *Opt. Lett.* **15**, 568-569 (1990).
10. P. D. Maker, and R. E. Muller, "Phase holograms in poly methyl methacrylate," J. Vac. Sci. Technol. B **10**, 2516-2519 (1992).
11. P. D. Maker and R. E. Muller, "Phase holograms in PMMA with proximity effect correction," NASA CP-3227, 207-221 (1993).
12. M. Larsson, M. Ekberg, F. Nikolajeff, and S. Hård, P. D. Maker, and R. E. Muller, "Proximity-compensated kinoforms directly written by E-beam lithography," SPIE Proc. **CR49** (1993).
13. P. D. Maker, D. W. Wilson, and R. E. Muller, "Fabrication and performance of optical interconnect analog phase holograms made by E-beam lithography," in Optoelectronic Interconnects and Packaging, R. T. Chen and P. S. Guilfoyle, eds., SPIE Proc. **CR62**, 415-430 (1996).
14. D. W. Wilson, P. D. Maker, and R. E. Muller, "Binary optic reflection grating for an imaging spectrometer," in Diffractive and Holographic Optics Technology III, SPIE Proc. **2689** (1996).
15. http://www.microchem.com/products/pmma.htm
16. http://www.microchem.com/products/pmgi.htm
17. D. J. Dougherty, R. E. Muller, P. D. Maker, and S. Forouhar, "Stitching-error reduction in gratings by shot-shifted electron-beam lithography," J. Lightwave Technology **19**, 1527 -1531 (2001).
18. Y. Muroya, T. Nakamura, H. Yamada, and T. Torikai, "Precise wavelength control for DFB laser diodes by novel corrugation delineation method," Photonics Technol. Lett. **9**, 288–290 (1997).
19. J. Albert, S. Thériault, F. Bilodeau, D. C. Johnson, K. O. Hill, P. Sixt, and M. J. Rooks, "Minimization of phase errors in long fiber Bragg grating phase masks made using electron beam lithography," Photonics Technol. Lett., **8** 1334–1336 (1996).
20. R. C. Tiberio, D. W. Carr, M. J. Rooks, S. J. Mihailov, F. Bilodeau, J. Albert, D. Strykman, D. C. Johnson, K. O. Hill, A. W. McClelland, and B. J. Hughes, "Fabrication of electron beam generated, chirped, phase mask (1070.11–1070.66 nm) for fiber Bragg grating dispersion compensator," J. Vac. Sci. Technol. B **16**, 3237–3240 (1998).